Available online at www.sciencedirect.com
ScienceDirect
Ceramics International 34 (2008) 1273–1278
CERAMICS INTERNATIONAL
www.elsevier.com/locate/ceramint

High-temperature proton conductor $Sr(Ce_{0.6}Zr_{0.4})_{0.9}Y_{0.1}O_{3-\delta}$: Preparation, sintering and electrical properties

Jingchao Zhang [a], Zhaoyin Wen [a,*], Shahua Huang [a], Jianguo Wu [b], Jinduo Han [a], Xiaoxiong Xu [a]

[a] Shanghai Institute of Ceramics, Chinese Academy of Sciences, 1295 DingXi Road, Shanghai 200050, PR China
[b] Department of Materials Science and Engineering, Tongji University, 1239 SiPing Road, Shanghai 200092, PR China

Received 9 January 2007; received in revised form 13 February 2007; accepted 10 March 2007
Available online 10 April 2007

Abstract

$Sr(Ce_{0.6}Zr_{0.4})_{0.9}Y_{0.1}O_{3-\delta}$ was prepared by a wet chemical route and the stages of its formation, as well as the characterization of the resulting compounds were carried out using TG–DTA, XRD, TEM, SEM and EPMA techniques. Experimental results indicate that a calcination temperature of 900–1100 °C, which is much lower than that for the conventional solid state reaction process, is sufficient to the formation of single perovskite phase. $Sr(Ce_{0.6}Zr_{0.4})_{0.9}Y_{0.1}O_{3-\delta}$ powders obtained are fine, narrowly distributed and well crystallized. This strongly improves the sinter properties and the formation of a dense $Sr(Ce_{0.6}Zr_{0.4})_{0.9}Y_{0.1}O_{3-\delta}$. Sintered at $T \geq 1350$ °C, samples with density ≥97.16% of the theoretical could be obtained. In addition, the proton conductivities of $Sr(Ce_{0.6}Zr_{0.4})_{0.9}Y_{0.1}O_{3-\delta}$ ceramic were measured by impedance spectroscopy in 5% H_2/Ar and the evolution of the spectra with increasing temperature was analyzed.

Keywords: A. Sintering; B. X-ray methods; C. Impedance; D. Perovskites

1. Introduction

Several perovskite-type ceramics exhibit protonic conduction in humid or hydrogen-containing atmospheres at elevated temperatures. These materials have attracted considerable attention because of their potential applications as electrolytes in hydrogen pumps [1], gas sensors [2–4], steam electrolyzers [5], solid oxide fuel cells (SOFCs) [6–8], membrane separators and membrane reactors [9–11]. A typical example of proton conducting ceramics of this class is the substituted solid solution material based on the perovskite oxide $SrCeO_3$, $SrCe_{0.9}Y_{0.1}O_{3-\delta}$. It is superior with respect to its transport number of protons while it lacks mechanical and chemical stability (e.g., carbonate formation) [12]. Several studies suggest that the partial substitution of Zr^{4+} for Ce^{4+} can improve mechanical and chemical stability of $SrCe_{0.9}Y_{0.1}O_{3-\delta}$ [13–15].

In general, applications of the conducting ceramics always start with the synthesis of the corresponding powders [16]. Highly disagglomerated, fine powders are of particular interest because of their low-temperature sinterability and compositional homogeneity, which are essential for obtaining high-performance ceramics [17]. However, $SrCe_{0.9}Y_{0.1}O_{3-\delta}$ powders have been mostly prepared by solid state reaction process requiring a temperature of at least 1200 °C and longer annealing time, with intermediate ZrO_2 ball milling. As a consequence, uncontrolled crystalline growth may occur, which could induce chemical and grain-size non-uniformity. Compared to solid state reaction process, the wet chemical route is preferable for many ceramic systems [18]. The homogeneity of the product is expected to increase because mixing of the reagents occurs at the molecular level. The resulting powders have a high specific surface area and, consequently, a high reactivity, which decreases the final treating temperature and the time of synthesis [19]. The most attractive, this method offers the possibility of good compositional control in a multi-component system [20].

From this viewpoint, the present work was to find a wet chemical route for avoiding the drawbacks of the conventional solid state reaction process and preparing homogeneous fine $Sr(Ce_{0.6}Zr_{0.4})_{0.9}Y_{0.1}O_{3-\delta}$ material. The evolution of crystalline

* Corresponding author. Tel.: +86 21 52411704; fax: +86 21 52413903.
E-mail address: zywen@mail.sic.ac.cn (Z. Wen).

0272-8842/$34.00
doi:10.1016/j.ceramint.2007.03.007

phase as well as the characteristics of the powders has been investigated in detail. It was also of interest to investigate the sintering and electrical properties of $Sr(Ce_{0.6}Zr_{0.4})_{0.9}Y_{0.1}O_{3-\delta}$ ceramic.

2. Experimental

2.1. Sample preparation

$Sr(Ce_{0.6}Zr_{0.4})_{0.9}Y_{0.1}O_{3-\delta}$ was prepared by the following wet chemical route. $Sr(NO_3)_2$ (AR), $Ce(NO_3)_3{\cdot}6H_2O$ (AR), $Zr(NO_3)_4{\cdot}5H_2O$ (AR) and $Y(NO_3)_3{\cdot}6H_2O$ (AR) were mixed in the stoichiometric ratio with citric acid in distilled water to form a 0.2 M solution of total metal ions. The amount of citric acid was three times the total molar amount of the metal ions. The mixture was adjusted to have a pH value of 8 by ammonia solution. The resulting solution was stirred and heated at 70 °C until a viscous liquid was obtained. After drying at 70 °C and 150 °C, respectively, the gel-like material became sponge-like and brittle. It was then heated to 350 °C for 4 h. The resulting material was ground with an agate mortar and calcined in the temperature range of 500–1100 °C for 5 h to study its crystallization behavior. $Sr(Ce_{0.6}Zr_{0.4})_{0.9}Y_{0.1}O_{3-\delta}$ powders obtained were then milled in a planetary ball mill, shaped into disks by isostatic pressing under 200 MPa and finally sintered between 1150 and 1550 °C for 10 h in air.

2.2. Characterization techniques

The thermal decomposition process of the $Sr(Ce_{0.6}Zr_{0.4})_{0.9}Y_{0.1}O_{3-\delta}$ precursor was studied in air by thermogravimetric (TG) and differential thermal analyses (DTA) at a heating rate of 10 K min^{-1} from room temperature to 1300 °C.

Phase characterization of powders and ceramics was performed by X-ray diffraction analysis (Rigaku RAD-C, 12 kW) at room temperature using Cu Kα radiation in the 2θ range from 5° to 80°. High-purity silicon powders were used as an internal standard to determine the lattice parameters.

Morphology of powders was assessed by transmission electron microscope (TEM, JEOL, JEM-2100F) and a field-emission scanning electron microscope (FESEM, JEOL, JSM-6700F). Microstructures of the sintered ceramics were observed by electron probe X-ray microanalyzer (EPMA, JEOL, JXA-8100).

Density measurements of the sinters were obtained by the Archimedes method with ethanol as the immersing media. The theoretical density of the sinters was based on the equation:

$$T_d = \frac{ZM_C}{V_C N_A} \quad (1)$$

where Z is the number of chemical species in the unit cell, M_C the molar mass of a single chemical species corresponding to the chemical formula (g mol^{-1}), V_C the unit cell volume (A^3) and N_A is the Avogadro's number (6.0221×10^{23} mol^{-1}) [21].

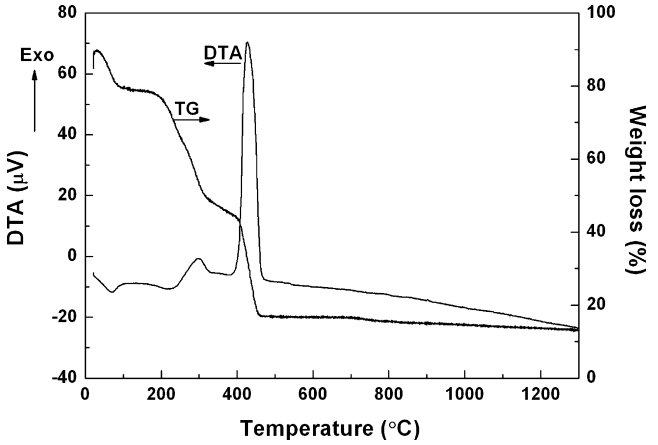

Fig. 1. TG/DTA curves of the $Sr(Ce_{0.6}Zr_{0.4})_{0.9}Y_{0.1}O_{3-\delta}$ precursor in air.

2.3. Electrical measurements

Sintered disks were polished and then cleaned with ethanol in an ultrasonic cleaner. Pt electrodes were formed by painting the planar faces of the disks with platinum paste and then baking at 800 °C for 1 h. Impedance measurements were performed over wide temperature in the frequency range of 10^{-2} to 10^6 Hz in 5% H_2/Ar using a Solartron 1260 frequency response analyzer.

3. Results and discussion

3.1. Crystallographic and morphological evolution

The thermal decomposition process of the $Sr(Ce_{0.6}Zr_{0.4})_{0.9}Y_{0.1}O_{3-\delta}$ precursor was recorded by TG and DTA as shown in

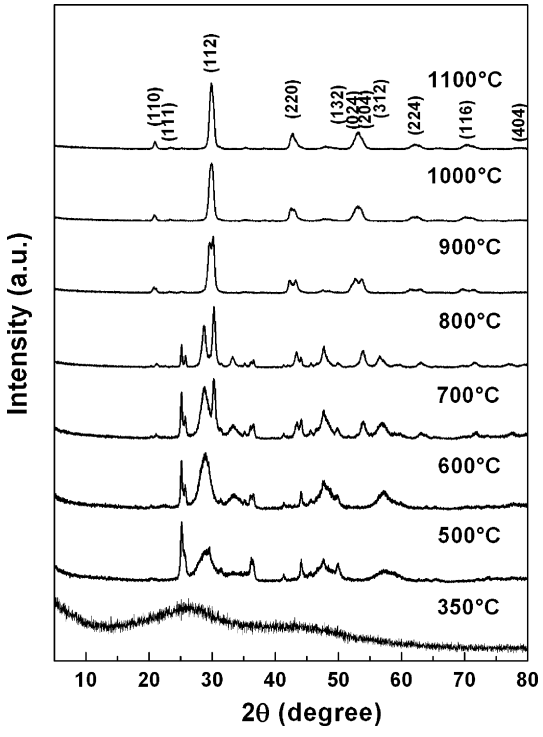

Fig. 2. XRD patterns of the powders calcined at various temperatures.

Fig. 1. It can be seen that the thermal decomposition process consists of four stages. The first one, 11.86% weight loss between room temperature and 120 °C corresponding to a slight endothermic peak is attributed to the loss of water. The second one, a fast weight loss stage claimed about 34.34% in the temperature range of 135–350 °C indicated by an exothermic peak around 295 °C on the DTA curve, is due to the thermal decomposition of the citrate complex. The third stage from 360 to 500 °C about 33.91% weight loss, results from the combustion of remaining organic components, corresponding to a violent exothermic peak at 427 °C on the DTA curve. The last one is a gradual weight loss stage, with not too obvious weight loss between 700 and 800 °C, is probably related to the thermal decomposition of carbonate.

The development of the crystalline phase as a function of calcination temperature is illustrated by the XRD patterns plotted in Fig. 2. The product obtained below 350 °C is primarily amorphous in structure. At 500 °C, the powders have crystallized. Powders calcined at 500, 600, 700 and 800 °C are mainly composed of carbonates ($SrCO_3$) and oxides (CeO_2). When the calcination temperature is increased to 900 °C, $Sr(Ce_{0.6}Zr_{0.4})_{0.9}Y_{0.1}O_{3-\delta}$ phase is observed. Further enhancement of calcination temperature increases the purity and peak intensity of the perovskite phase. The synthesis temperature of $Sr(Ce_{0.6}Zr_{0.4})_{0.9}Y_{0.1}O_{3-\delta}$ phase is about 1100 °C, which is much lower than that of the conventional solid state reaction process [13]. This decrease of synthesis temperature may be due to the higher reactivity of the powders synthesized by the wet chemical route.

Fig. 3 gives the TEM and SEM images of the powders. As shown in Fig. 3(a) and (b), the particle size of the sample is small and homogeneous, which consists of nanometer particles whose crystalline facets are relatively well-defined. Fig. 3(c) and (d) shows the morphological evolution of the powders as a function of calcination temperature. It can be seen that the particle size tends to increase with calcination temperature. However, the grains remain remarkably small (<0.3 μm) and in relatively homogeneous distribution up to 1000 °C.

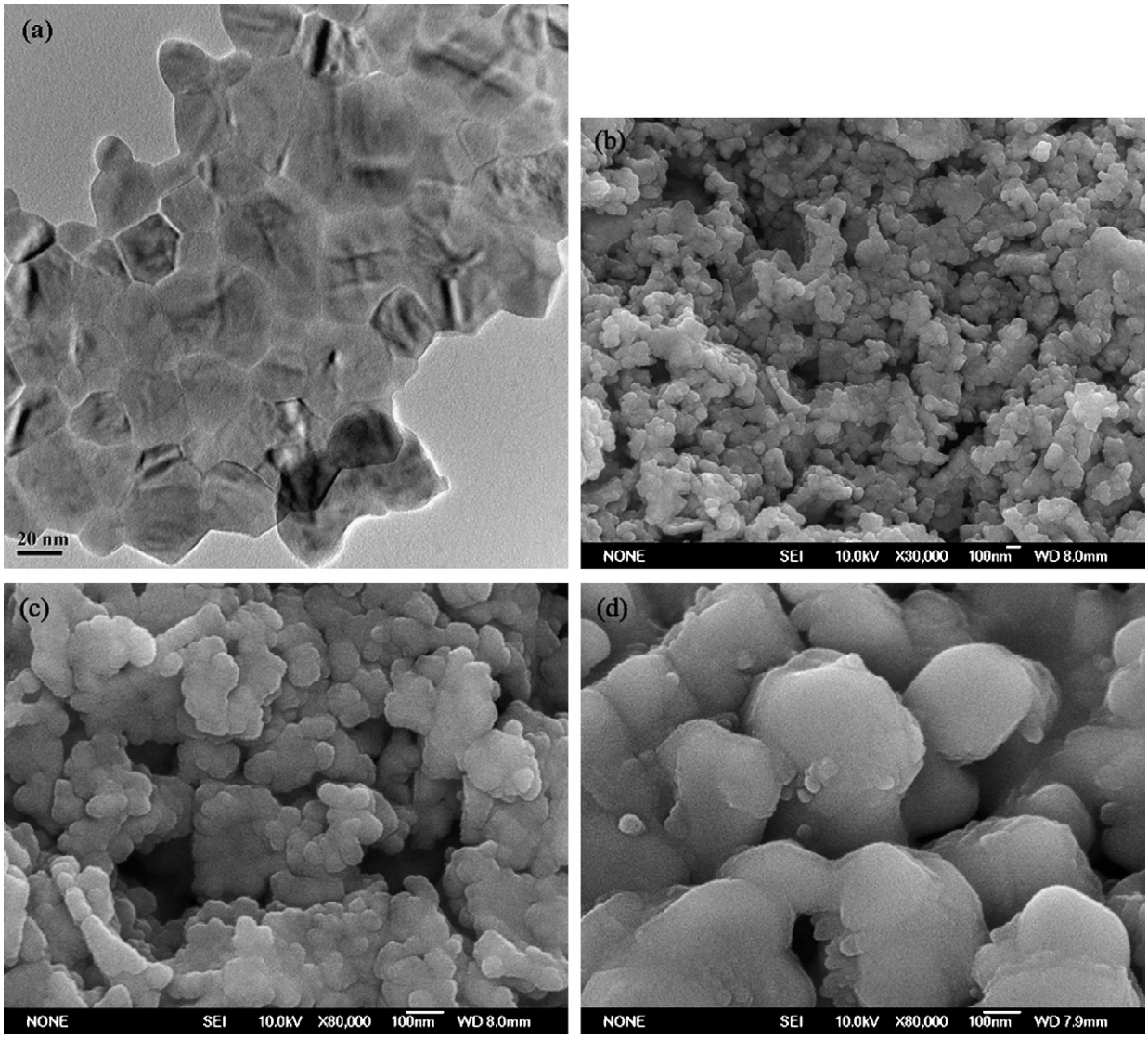

Fig. 3. Morphology of $Sr(Ce_{0.6}Zr_{0.4})_{0.9}Y_{0.1}O_{3-\delta}$ powders: (a) TEM, 900 °C; (b and c) SEM, 900 °C; (d) SEM, 1000 °C.

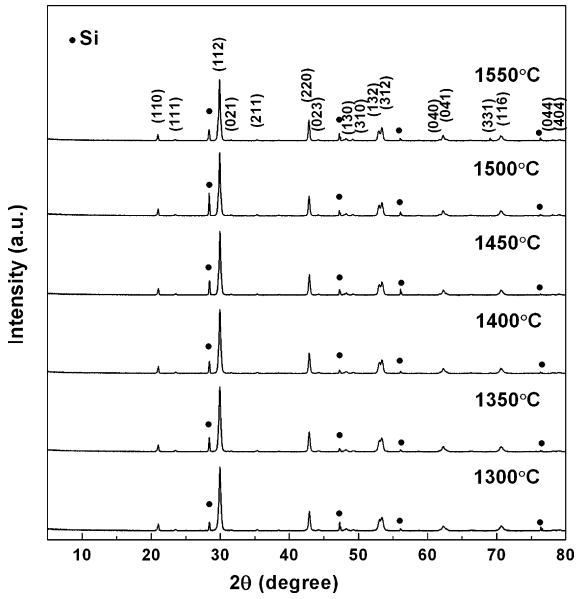

Fig. 4. XRD patterns of $Sr(Ce_{0.6}Zr_{0.4})_{0.9}Y_{0.1}O_{3-\delta}$ ceramics sintered at various temperatures.

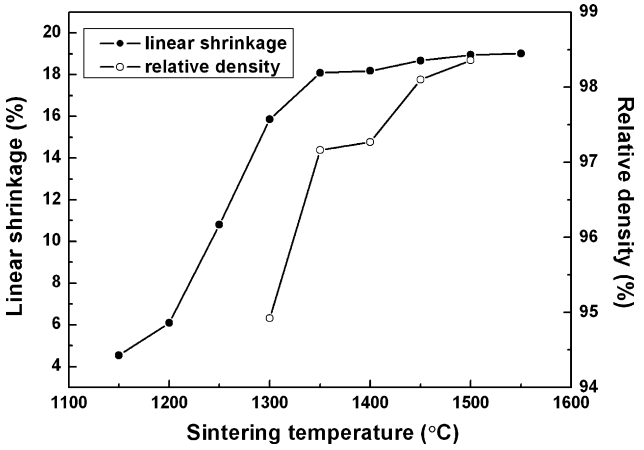

Fig. 5. Effects of sintering temperature on linear shrinkage and relative density of $Sr(Ce_{0.6}Zr_{0.4})_{0.9}Y_{0.1}O_{3-\delta}$ disks.

3.2. Sintering behavior

Fig. 4 shows the XRD patterns of $Sr(Ce_{0.6}Zr_{0.4})_{0.9}Y_{0.1}O_{3-\delta}$ ceramics sintered at various temperatures. After sintered at 1300, 1350, 1400, 1450, 1500 and 1550 °C, respectively, the samples all present well crystallized perovskite-type structure. Except

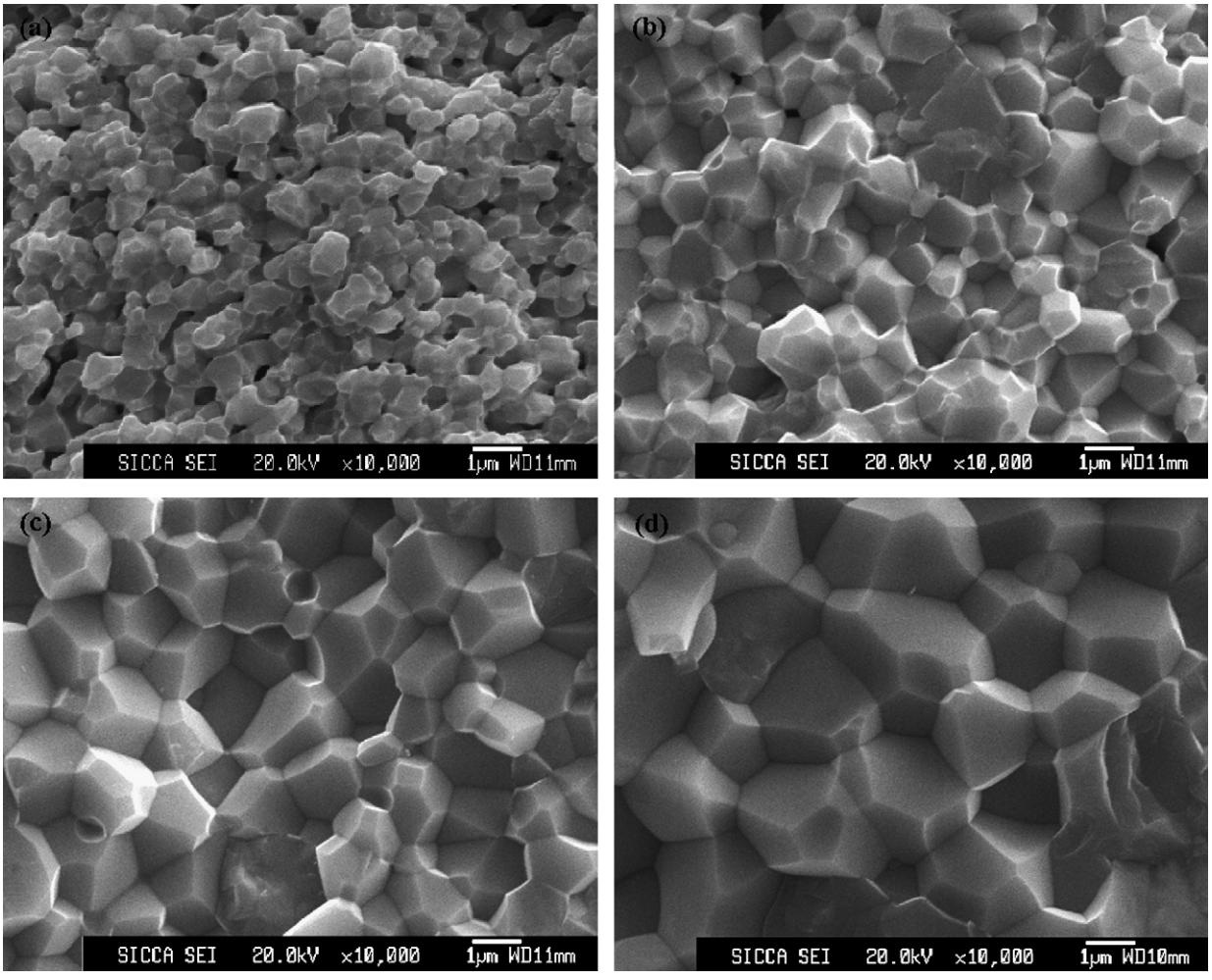

Fig. 6. Microstructure of fractured ceramics sintered at different temperatures: (a) 1300 °C; (b) 1350 °C; (c) 1400 °C; (d) 1450 °C.

internal standard silicon, no evidence for impurity phases is observed. It demonstrates that $Sr(Ce_{0.6}Zr_{0.4})_{0.9}Y_{0.1}O_{3-\delta}$ powders prepared by the wet chemical route can be successfully sintered into single phase at lower temperature.

The linear shrinkage of $Sr(Ce_{0.6}Zr_{0.4})_{0.9}Y_{0.1}O_{3-\delta}$ disks is calculated by measuring the diameter of the disks before and after sintering. Fig. 5 gives effects of sintering temperature on linear shrinkage and relative density of $Sr(Ce_{0.6}Zr_{0.4})_{0.9}Y_{0.1}O_{3-\delta}$ disks. Below 1200 °C, the linear shrinkage is low. In the temperature range of 1200–1350 °C, the linear shrinkage increase rapidly from 6.09% to 18.09%. From 1350 to 1550 °C the linear shrinkage continue increasing, but it exhibits no tremendous change. Increasing sintering temperature also increases relative density of $Sr(Ce_{0.6}Zr_{0.4})_{0.9}Y_{0.1}O_{3-\delta}$ ceramics. Between 1300 and 1350 °C, the relative density of samples has rapid increase. When the sintering temperature exceeds 1350 °C, $Sr(Ce_{0.6}Zr_{0.4})_{0.9}Y_{0.1}O_{3-\delta}$ compacts can be sintered to a density higher than 97% of the theoretical. Sintering at 1450 and 1500 °C for 10 h result in a density of 98.1 and 98.36%, respectively.

Fig. 6 is EPMA images of fractured surfaces of $Sr(Ce_{0.6}Zr_{0.4})_{0.9}Y_{0.1}O_{3-\delta}$ ceramics sintered at 1300–1450 °C for 10 h, which clearly shows the effects of sintering temperature on the densification, microstructure and grain growth. The grain size increases with sintering temperature increasing. However, the grains remain relatively small and in homogeneous distribution up to 1450 °C. In addition, the higher the sintering temperature, the higher the sample density. It can be seen that the sample sintered at 1300 °C is porous, while the ceramics sintered in the temperature range of 1350–1450 °C are much denser and have a similar microstructure. With an increase in sintering temperature, the fracture characteristics of the samples change from intergranular to transgranular fracture.

Considering results above, 1450 °C is selected as the ultimate sintering temperature. It is regarded that the fine particle morphology of the powders synthesized by the wet chemical route is responsible for its higher sinterability and higher densification of $Sr(Ce_{0.6}Zr_{0.4})_{0.9}Y_{0.1}O_{3-\delta}$ ceramic.

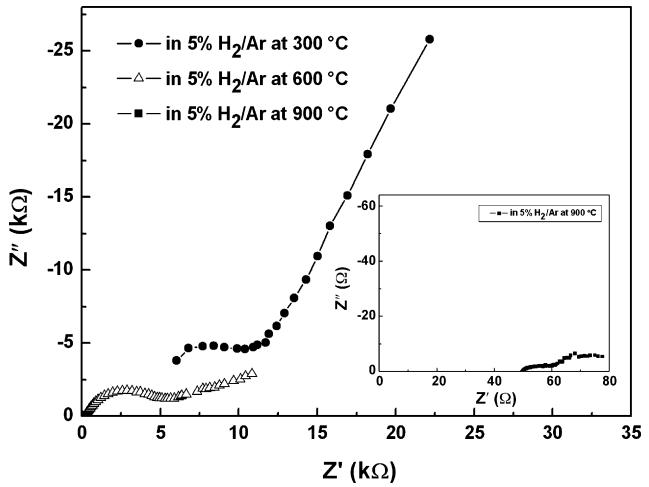

Fig. 7. Impedance spectra of $Sr(Ce_{0.6}Zr_{0.4})_{0.9}Y_{0.1}O_{3-\delta}$ ceramic in 5% H_2/Ar at different temperatures.

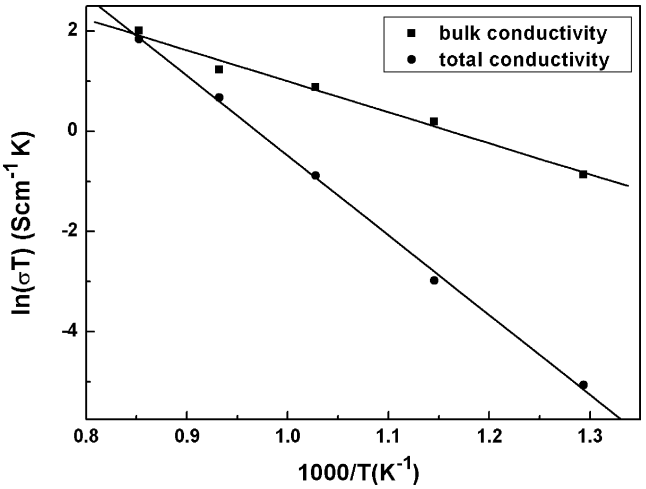

Fig. 8. Arrhenius plots of the bulk and total conductivities of $Sr(Ce_{0.6}Zr_{0.4})_{0.9}Yb_{0.1}O_{3-\delta}$ ceramic in 5% H_2/Ar.

3.3. Electrical properties

It is important for the data analysis to consider the evolution of the spectra with increasing temperature [22]. Representative impedance spectra are shown in Fig. 7, where the imaginary part of the impedance, Z'', is plotted versus its real part, Z', for $Sr(Ce_{0.6}Zr_{0.4})_{0.9}Y_{0.1}O_{3-\delta}$ ceramic in 5% H_2/Ar at 300, 600 and 900 °C. At 300 °C, the spectrum consists of two semicircles corresponding to the conduction in the grains and across the grain boundaries, respectively, where the second is large, slightly depressed. With increasing temperature, the first semicircle could not be observed due to the low bulk capacity [23], while the second semicircle shrinks, and a tail which is related to processes occurring at the electrodes appears. When the temperature is increased to 900 °C, the second semicircle and electrode tail overlapped more or less. The bulk and total resistances can be determined from the high frequency intercept and the low frequency intercept of the second semicircle with the real axis. As the temperature is increased, the bulk resistance decreases as well as the total resistance.

The bulk and total conductivities are calculated from the respective R-values using the bulk dimensions of the sample (diameter d and surface S): $\sigma = d/(R \times S)$ [24]. The activation energy for electrical conduction, E, is determined by plotting $\ln \sigma T$ versus $1000/T$ using the Arrhenius equation of $\ln \sigma T = \ln A - (E/RT)$. Fig. 8 shows the Arrhenius plots of the bulk and total conductivities of $Sr(Ce_{0.6}Zr_{0.4})_{0.9}Y_{0.1}O_{3-\delta}$ ceramic in 5% H_2/Ar. The slope of the line is almost linear, which indicates the constancy of the conduction mechanism. At 900 °C, the maximum bulk and total conductivities of $Sr(Ce_{0.6}Zr_{0.4})_{0.9}Y_{0.1}O_{3-\delta}$ ceramic are 6.36×10^{-3} and 5.37×10^{-3} S cm^{-1}, respectively, which are of the same order of magnitude as the reported values of $SrCe_{0.9}Y_{0.1}O_{3-\delta}$ ceramic obtained by Iwahara et al. [25].

4. Conclusions

$Sr(Ce_{0.6}Zr_{0.4})_{0.9}Y_{0.1}O_{3-\delta}$ proton conductor was prepared by a wet chemical route. A single phase with a well-defined

perovskite-type structure was obtained. The synthesized $Sr(Ce_{0.6}Zr_{0.4})_{0.9}Y_{0.1}O_{3-\delta}$ powders are fine, narrowly distributed, and well crystallized. The high reactivity of the powders is reflected in the formation and densification of pure perovskite $Sr(Ce_{0.6}Zr_{0.4})_{0.9}Y_{0.1}O_{3-\delta}$ ceramic. A relative density higher than 97% is easy to obtain at 1350 °C, which is remarkably lower than the conventional solid state process. According to impedance measurements, the conductivity of $Sr(Ce_{0.6}Zr_{0.4})_{0.9}Y_{0.1}O_{3-\delta}$ ceramic as high as 5.37×10^{-3} S cm^{-1} at 900 °C in 5% H_2/Ar was realized which was of the same order of magnitude as the reported values of $SrCe_{0.9}Y_{0.1}O_{3-\delta}$ ceramic.

Acknowledgements

We are grateful to the support of National Research Program 05-087 on this work. Ms. Zhonghua Gu and Mr. Xiaohe Xu are acknowledged for their help in the experiment.

References

[1] H. Matsumoto, S. Hamajima, T. Yajima, H. Iwahara, Electrochemical hydrogen pump using $SrCeO_3$-based proton conductor: effect of water vapor at the cathode on the pumping capacity, J. Electrochem. Soc. 148 (10) (2001) D121–D124.

[2] T. Yajima, K. Koide, H. Takai, N. Fukatsu, H. Iwahara, Application of hydrogen sensor using proton conductive ceramics as a solid electrolyte to aluminum casting industries, Solid State Ionics 79 (1995) 333–337.

[3] N. Fukatsu, N. Kurita, K. Koide, T. Ohashi, Hydrogen sensor for molten metals usable up to 1500 K, Solid State Ionics 113–115 (1998) 219–227.

[4] T. Schober, Applications of oxidic high-temperature proton conductors, Solid State Ionics 162–163 (2003) 277–281.

[5] H. Iwahara, Technological challenges in the application of proton conducting ceramics, Solid State Ionics 77 (1995) 289–298.

[6] N. Taniguchi, E. Yasumoto, T. Gamo, Operating properties of solid oxide fuel cells using $BaCe_{0.8}Gd_{0.2}O_{3-\alpha}$ electrolyte, J. Electrochem. Soc. 143 (6) (1996) 1886–1890.

[7] D. Hassan, S. Janes, R. Clasen, Proton-conducting ceramics as electrode/electrolyte materials for SOFC's. Part I. Preparation, mechanical and thermal properties of sintered bodies, J. Eur. Ceram. Soc. 23 (2) (2003) 221–228.

[8] T. Shimada, C. Wen, N. Taniguchi, J. Otomo, H. Takahashi, The high temperature proton conductor $BaZr_{0.4}Ce_{0.4}In_{0.2}O_{3-\delta}$, J. Power Sources 131 (1–2) (2004) 289–292.

[9] S. Hamakawa, T. Hibino, H. Iwahara, Electrochemical methane coupling using protonic conductors, J. Electrochem. Soc. 140 (2) (1993) 459–462.

[10] G. Karagiannakis, S. Zisekas, M. Stoukides, Hydrogenation of carbon dioxide on copper in a H^+ conducting membrane-reactor, Solid State Ionics 162–163 (2003) 313–318.

[11] S.G. Cheng, V.K. Gupta, J.Y.S. Lin, Synthesis and hydrogen permeation properties of asymmetric proton-conducting ceramic membranes, Solid State Ionics 176 (35–36) (2005) 2653–2662.

[12] T. Yajima, H. Kazeoka, T. Yogo, H. Iwahara, Proton conduction in sintered oxides based on $CaZrO_3$, Solid State Ionics 47 (3–4) (1991) 271–275.

[13] T. Matzke, M. Cappadonia, Proton conductive perovskite solid solutions with enhanced mechanical stability, Solid State Ionics 86–88 (1996) 659–663.

[14] K.H. Ryu, S.M. Haile, Chemical stability and proton conductivity of doped $BaCeO_3$–$BaZrO_3$ solid solutions, Solid State Ionics 125 (1–4) (1999) 355–367.

[15] N. Taniguchi, T. Kuroha, C. Nishimura, K. Iijima, Chemical stability and proton conductivity of doped $BaCeO_3$–$BaZrO_3$ solid solutions, Solid State Ionics 176 (39–40) (2005) 2979–2983.

[16] M. Anilkumar, R. Pasricha, V. Ravi, Synthesis of bismuth oxide nanoparticles by citrate gel method, Ceram. Int. 31 (6) (2005) 889–891.

[17] A. Sin, B.E. Montaser, P. Odier, Synthesis and sintering of large batches of barium zirconate nanopowders, J. Am. Ceram. Soc. 85 (8) (2002) 1928–1932.

[18] C.Y. Chung, Y.H. Chang, G.J. Chen, Y.L. Chai, Preparation, structure and ferroelectric properties of $Ba(Fe_{0.5}Nb_{0.5})O_3$ powders by sol–gel method, J. Crystal Growth 284 (1–2) (2005) 100–107.

[19] A. Sin, P. Odier, Gelation by acrylamide, a quasi-universal medium for the synthesis of fine oxide powders for electroceramic applications, Adv. Mater. 12 (9) (2000) 649–652.

[20] D. Dionysiou, X.W. Qi, Y.S. Lin, G. Meng, D. Peng, Preparation and characterization of proton conducting terbium doped strontium cerate membranes, J. Membr. Sci. 154 (2) (1999) 143–153.

[21] N. Sammes, R. Phillips, A. Smirnova, Proton conductivity in stoichiometric and sub-stoichiometric yittrium doped $SrCeO_3$ ceramic electrolytes, J. Power Sources 134 (2) (2004) 153–159.

[22] K.D. Kreuer, Aspects of the formation and mobility of protonic charge carriers and the stability of perovskite-type oxides, Solid State Ionics 125 (1–4) (1999) 285–302.

[23] B. Groß, S. Marion, R. Hempelmann, D. Grambole, F. Herrmann, Proton conducting $Ba_3Ca_{1.18}Nb_{1.82}O_{8.73}/H_2O$: sol–gel preparation and pressure/composition isotherms, Solid State Ionics 109 (1–2) (1998) 13–23.

[24] F.M.M. Snijkers, A. Buekenhoudt, J. Cooymans, J.J. Luyten, Proton conductivity and phase composition in $BaZr_{0.9}Y_{0.1}O_{3-\delta}$, Scripta Mater. 50 (5) (2004) 655–659.

[25] H. Iwahara, T. Esaka, H. Uchida, N. Maeda, Proton conduction in sintered oxides and its application to steam electrolysis for hydrogen production, Solid State Ionics 3–4 (1981) 359–363.